Superconductivity in $Y_7Ru_4InGe_{12}$

Jin-Ke Bao,[1,*] Daniel E. Bugaris,[1,*] Huihuo Zheng,[2] Kristin Willa,[1] Ulrich Welp,[1] Duck Young Chung,[1] and Mercouri G. Kanatzidis[1,3,†]

[1]*Materials Science Division, Argonne National Laboratory, Argonne, Illinois 60439, USA*
[2]*Leadership Computing Facility, Argonne National Laboratory, Argonne, Illinois 60439, USA*
[3]*Department of Chemistry, Northwestern University, Evanston, Illinois 60208, USA*

(Received 28 November 2018; published 12 February 2019)

We report a type-II intermetallic superconductor $Y_7Ru_4InGe_{12}$ with a transition temperature (T_c) of ∼5.8 K, which is confirmed by zero resistivity, diamagnetic magnetic susceptibility, and specific-heat jump. Single crystals of $Y_7Ru_4InGe_{12}$ were grown from a reactive indium flux. $Y_7Ru_4InGe_{12}$ crystallizes in the tetragonal space group $P4/m$ and features a $[Ru_4InGe_{12}]$ polyanionic network with Y atoms located in three different channels. The upper critical fields of $Y_7Ru_4InGe_{12}$ at 0 K are determined to be ∼5.3 and 2.4 T along the c axis and the ab plane, respectively. The estimated coherence length along the c axis (∼174 Å) is much larger than the estimated mean free path along the c axis (∼29 Å) in $Y_7Ru_4InGe_{12}$, placing its superconductivity in the so-called dirty regime. The compound exhibits a large superconducting specific-heat jump $\frac{\Delta C}{\gamma_e T_c} \approx 2.4$, significantly well above the weak-coupling Barden-Cooper-Schrieffer theoretical value of 1.43 and pointing to a strong-coupling scenario in $Y_7Ru_4InGe_{12}$. Density-functional-theory calculations show that the density of states in $Y_7Ru_4InGe_{12}$ exhibits a broad peak near the Fermi level which mainly derives from Y-4d, Ru-4d, and Ge-4p states.

DOI: 10.1103/PhysRevMaterials.3.024802

I. INTRODUCTION

In 1911, superconductivity, as a quantum phenomenon, was first discovered in mercury [1]. Until 1957, the Bardeen-Cooper-Schrieffer (BCS) theory, based on the framework of Cooper pair and electron-phonon coupling, had been successfully proposed to explain this phenomenon [2]. However, up to now, there is still no effective theory available to help us predict superconductivity in a certain material even if it is conventional [3]. Furthermore, different types of mechanisms appear to exist for different superconducting families [4], such as unconventional high-T_c cuprates [5] and iron-based pnictides [6], as well as intermetallics (e.g., heavy fermion superconductor $CeCu_2Si_2$ [7]), all of which are still under debate [8,9]. Thus, exploring new superconducting materials with atypical structures is important, as it serves to provide an additional understanding of the unresolved mechanism of superconductivity. Intermetallic compounds containing rare-earth, transition-metal, and germanium elements cover a large phase space. Electron correlation, bandwidth, and spin-orbit coupling in those compounds can be tuned across the transition-metal elements [10]. The interplay between local magnetic moments and conduction electrons can also be investigated by introducing 4f electrons from the rare-earth elements. As a result, the existence of 4f, d, and p electrons in those compounds provides a platform to create different orders such as charge density wave (e.g., $R_2Ru_3Ge_5$, R = Pr, Sm, Dy) [11], itinerant ferromagnetism from 3d electrons (e.g., $RCrGe_3$, R = La-Nd, Sm) [12], and complex magnetism from both 3d and 4f electrons (e.g., $SmMn_2Ge_2$) [13]. There are several interesting superconductors discovered in this phase space too. For instance, YFe_2Ge_2 with the $ThCr_2Si_2$-type structure exhibits unconventional superconductivity at 1.8 K with a large value of the Sommerfeld coefficient, indicating significant electron correlations in this system [14]. The filled skutterudite $PrPt_4Ge_{12}$ is a moderately strong-coupling superconductor at 7.9 K with pointlike nodes in the superconducting gap function [15,16]. $Lu_4T_3Ge_{13-x}$ (T = Co, Rh, Os, Ru) form a family of superconductors with strong site disorders and low carrier concentrations [17,18]. A heavy fermion intermetallic $CeCu_2Ge_2$ exhibits unconventional superconductivity [19] which is believed to be located around a quantum critical point [20] where its incommensurate antiferromagnetic order is continuously suppressed by physical pressure. There are indeed plenty of areas not yet fully investigated in this phase space where it is possible to discover new materials including superconductors.

Molten metal flux enhances the diffusion of refractory metals and alloys and overcomes activation barriers by dissolving them. As a result, low-melting indium is often used in intermetallic systems as a flux not only to grow crystals of known phases [21,22] but also to perform exploratory synthesis [22–24]. Indium can act as a reactive flux and be incorporated into the product crystals, which adds another dimension to the phase space. Here we report a superconducting compound $Y_7Ru_4InGe_{12}$ grown in a reactive In flux with a critical temperature of ∼5.8 K as determined by resistivity, magnetization, and specific-heat measurements.

*These authors contributed equally to this work.
†Corresponding author: m-kanatzidis@northwestern.edu

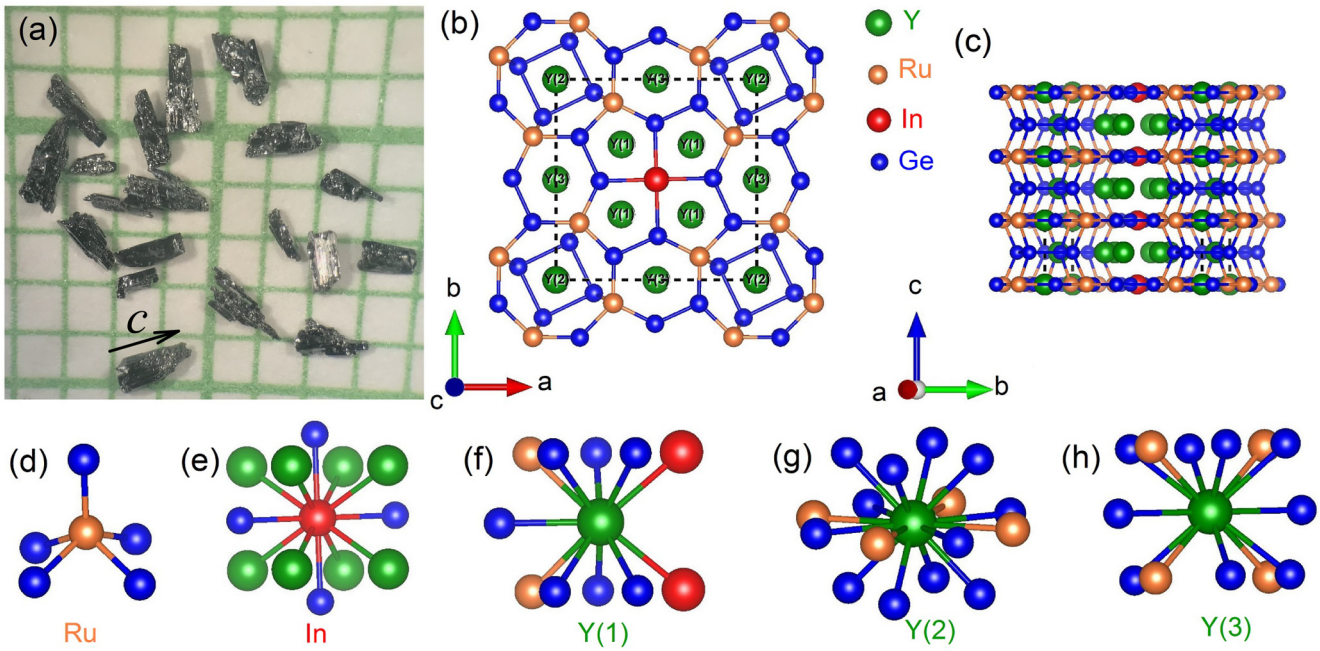

FIG. 1. (a) An image of $Y_7Ru_4InGe_{12}$ crystals on a 1-mm-grid paper under the optical microscope. The longest dimension in the rodlike crystal is along the *c* axis, as indicated by the arrow. (b),(c) Crystal structure of $Y_7Ru_4InGe_{12}$ viewed along and perpendicular to the [001] direction, respectively. The dashed lines represent the unit cell of the lattice in $Y_7Ru_4InGe_{12}$. (d)–(h) Coordination environments of the atoms Ru, In, Y(1), Y(2), and Y(3), respectively.

II. EXPERIMENTAL AND THEORETICAL METHODS

A. General details

Ruthenium powder (Johnson Matthey, 99.999+%) and yttrium pieces (Lunex, 99.98+%) were used as received. Germanium pieces (Plasmaterials, 99.999%) were ground to a fine powder prior to use. Indium shot (Apache Chemicals, 99.999%) was briefly rinsed with dilute HCl to remove a thin layer of oxide impurities on the surface. The handling of all materials was performed in an M-Braun glovebox under an inert Ar atmosphere (<0.1 ppm H_2O and O_2).

B. Crystal growth of $Y_7Ru_4InGe_{12}$

The atomic ratio Y : Ru : Ge : In = 7 : 4 : 12 : 63 was adopted in the reaction and crystal growth. The reaction mixture consisting of yttrium (0.2929 g, 3.29 mmol), ruthenium (0.1903 g, 1.88 mmol), germanium (0.4102 g, 5.65 mmol), and indium flux (3.4037 g, 29.65 mmol) was loaded into an alumina crucible. Next, the alumina crucible was covered by a stainless frit and placed in a 15 mm O.D. × 13 mm I.D. fused-silica tube and flame sealed under a vacuum of $<10^{-4}$ mbar. In a programmable furnace, the tube was heated to 1000 °C in 10 h, held at 1000 °C for 12 h, cooled to 500 °C at a rate of 2 °C/h, where the tube was removed from the furnace and centrifuged to filter molten In flux. Any remaining In metal was removed by soaking the product in dilute HCl (1 : 3 H_2O), followed by rinsing with H_2O and acetone. $Y_7Ru_4InGe_{12}$ formed as rodlike crystals with dimensions as large as 1 × 1 × 2 mm^3 [Fig. 1(a)]. The yield of $Y_7Ru_4InGe_{12}$ from this crystal growth experiment is ∼95% with a small amount of ternary phase containing Y, Ru, and Ge.

C. Scanning electron microscopy

The microprobe analysis of several crystals was performed with a Hitachi S-4700-II Scanning Electron Microscope equipped with an energy-dispersive x-ray spectrometer (EDS). The spectrometer utilizes an XFlash detector 6|60 from Bruker Nano GmbH and data were acquired with a beam current of 10 μA at 20 kV accelerating potential. Semiquantitative analysis by EDS on several crystals gives an average composition $Y_7Ru_{3.67(1)}In_{0.86(3)}Ge_{11.2(4)}$, consistent with the stoichiometric composition of $Y_7Ru_4InGe_{12}$.

D. Single-crystal x-ray diffraction

A single crystal was mounted on the tip of a glass fiber for x-ray diffraction. Intensity data were collected at 298 K using ω scans on a STOE 2T imaging plate diffraction system which uses the graphite-monochromatized Mo Kα radiation (λ = 0.71073 Å) and a 34-cm-diameter imaging plate. Individual frames were collected at 50 kV and 40 mA with a 4 min exposure time, and a 0.5° ω rotation. X-AREA, X-RED, and X-SHAPE software packages were used for data collection, integration, and analytical absorption corrections, respectively [25]. Structures were solved with the direct methods program SHELXS and refined with the full-matrix least-squares program SHELXL [26]. The final refinements included a secondary extinction correction. The parameters for data collection and details of the structure refinements are given in Table I. Atomic coordinates and thermal displacement parameters (U_{eq}) are given in Table S1 of the Supplemental Material (SM) [27], anisotropic thermal displacement parameters are given in Table S2 of the SM [27], and selected interatomic distances are given in Table S3 of the SM [27].

TABLE I. Crystallographic data and structure refinement details from single-crystal x-ray diffraction for $Y_7Ru_4InGe_{12}$.

Temperature (K)	298(2)
Wavelength (Å)	0.71073
Formula weight	2012.55
Crystal system	tetragonal
Space group	$P4/m$
a (Å)	10.5348(15)
c (Å)	4.2239(8)
Volume (Å^3)	468.78(13)
Z	1
ρ_c(g/cm^3)	7.129
μ(mm^{-1})	44.552
F(000)	882
Crystal size (mm^3)	0.430 × 0.053 × 0.045
θ range for data collection (deg)	3.87 to 34.99
Index ranges	$-17 \leqslant h \leqslant 17$
	$-17 \leqslant k \leqslant 14$
	$-6 \leqslant l \leqslant 5$
Reflections collected	7272
Independent reflections	1147[$R_{int} = 0.0391$]
Completeness to $\theta = 34.99°$	99.7%
Data/restraints/parameters	1147/0/40
GOF	1.225
Final R indices [$>2\sigma(I)$][a]	$R_{obs} = 0.0192$
	$wR_{obs} = 0.0412$
R indices (all data)[a]	$R_{all} = 0.0205$
	$wR_{all} = 0.0415$

[a]$R = \sum ||F_o| - |F_c|| / \sum |F_o|$, $wR = \{\Sigma[w(|F_o|^2 - |F_c|^2)^2] / \Sigma[w(|F_o|^4)]\}^{1/2}$ and calc $w = 1/[\sigma^2(F_o^2) + (0.0184 \times P)^2 + (0.4154 \times P)]$ where $P = (F_o^2 + 2F_c^2)/3$.

E. Powder x-ray diffraction

Phase purity of the products was confirmed by powder x-ray diffraction. The samples were finely ground and mounted on a flat Si-base sample holder. Data was collected on a PANalytical X'pert Pro diffractometer with a Ni-filtered Cu Kα source, operating at 45 kV and 40 mA under a continuous scanning method in the angular range 15–85° 2θ in steps of 0.0167°.

F. Magnetic susceptibility

Magnetic susceptibility measurements were carried out in a commercial magnetic property measurement system (MPMS3, Quantum Design). One small rodlike crystal was mounted on the quartz sample holder by a negligible amount of GE varnish. Magnetic fields were applied along and perpendicular to the rod direction. A small magnetic field (H = 10 Oe) was applied to measure the superconducting volume fraction. The demagnetization factor of the measured crystal (Fig. S1 in the SM [27]) was estimated as an ideal ellipsoid [28], which may lead to around 10% error in calculating the superconducting volume fraction. Magnetic fields were also calibrated by considering the demagnetization factor of the sample geometry in the field-dependent magnetization data at 2 K.

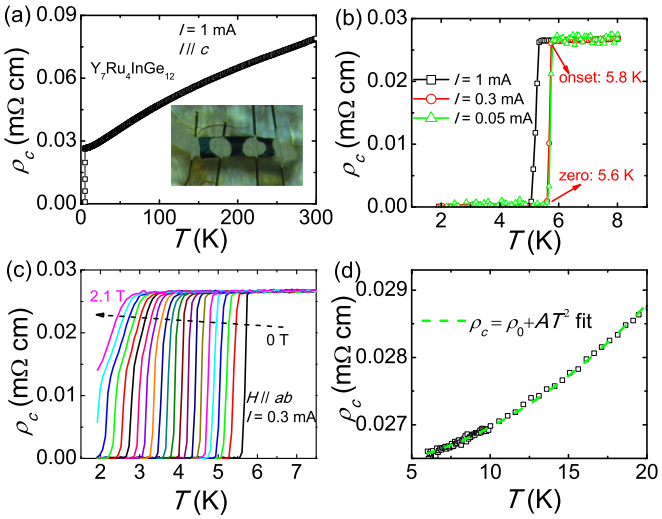

FIG. 2. (a) Temperature dependence of resistivity of $Y_7Ru_4InGe_{12}$ with the current (I = 1 mA) applied along the c axis. The inset shows the contacts for resistivity measurements. (b) Temperature dependence of resistivity of $Y_7Ru_4InGe_{12}$ across the superconducting transition under different currents. (c) Temperature dependence of the resistivity of $Y_7Ru_4InGe_{12}$ across the superconducting transition with varying magnetic fields from 0 to 2.1 T in 0.1 T steps. The magnetic fields are along the ab plane and the applied current is 0.3 mA. (d) Resistivity of $Y_7Ru_4InGe_{12}$ from 6 to 20 K and its power-law fit (green dashed line).

G. Transport properties

Transport-property measurements were done in a commercial physical property measurement system (DynaCool, Quantum Design). Crystals were polished into a regular rod shape before the measurements. The resistivity and Hall coefficient were measured by a four-probe method where gold wires were attached to the polished crystal by Dupont 4929N silver paste. The Hall coefficient was estimated by scanning the magnetic field from negative to positive values and subtracting the magnetoresistance component. The superconducting transition temperature is suppressed to a lower temperature when the applied current is increased to 1 mA, likely due to self-heating; see Fig. 2(b). Decreasing the current below 0.3 mA does not change the superconducting transition but increases the noise level, so we chose 0.3 mA for all further measurements of the transition. A current of 1 mA was applied to measure the resistivity of the sample over the whole temperature range of 2–300 K.

H. Specific heat

The ac specific-heat measurements were performed by a membrane-based (silicon nitride) ac nanocalorimeter [29,30]. One crystal with approximate dimensions 50 × 50 × 10 μm^3 was mounted onto the membrane with Apiezon grease and subsequently cooled down in vacuum. Measurements were carried out with a Synktex MCL1-540 multichannel lock-in system using operating frequencies ∼1 Hz. Specific-heat data were also collected in the DynaCool system by using a thermal relaxation method. Several $Y_7Ru_4InGe_{12}$ crystals with a total mass of 9.5 mg were mounted on the sample stage.

N grease was used to improve the thermal coupling between the crystals and the stage. Specific-heat data from these two different methods agree well with each other (Fig. S5 in the SM [27]).

I. Electronic structure calculation

Density-functional-theory (DFT) calculations were performed using the CRYSTAL package [31,32] with the Perdew-Burke-Ernzerhof (PBE) exchange-correlation functional. Pseudopotentials were employed to replace the 28 core electrons in each of Y, Ru, In, and Ge atoms [33,34]. The simulation was performed on the 24-atom primary unit cell. An 18 × 18 × 18 Monkhorst-Pack *k*-point grid was used to obtain a well-converged sampling of the first Brillouin zone.

III. RESULTS AND DISCUSSION

A. Synthetic route

Our initial attempt with a 4:5:10 (Y:Ru:Ge) ratio in a large excess of In (Y:In ≈ 1:10) at 1000 °C showed the formation of a quaternary phase, $Y_7Ru_4InGe_{12}$ (around 50% yield), in a form of black needle crystals along with black prismatic crystals of $Y_2Ru_3Ge_5$ [35] and minor phases of Ru_2Ge_3 and YRu_2Ge_2. The appearance of a large quantity of impurity phases as indicated by powder x-ray diffraction is mainly due to the off-stoichiometry of Y, Ru, and Ge compared to the target compound $Y_7Ru_4InGe_{12}$ in the initial composition. In this reaction, In not only serves as a flux, but is also incorporated into the structure to define the quaternary product. In order to increase the yield of the target phase $Y_7Ru_4InGe_{12}$, we modified the reaction by keeping the ratio of Y:Ru:Ge the same as the target phase and only changing the In flux ratio. For example, three different ratios of $Y : Ru : Ge : In = 7 : 4 : 12 : 7x$ ($x = 7$, 9, 19) can produce the quaternary phase $Y_7Ru_4InGe_{12}$, but yields and crystal sizes can vary. The fraction of $x = 19$ gave the lowest yields (∼5%) of $Y_7Ru_4InGe_{12}$, while $x = 9$ seems to be optimal in producing the largest crystals at the highest yield (∼95%) of the target compound $Y_7Ru_4InGe_{12}$. All $Y_7Ru_4InGe_{12}$ crystals used for physical property measurements in this paper are from the same batch with $x = 9$. Generally, due to the similar chemical nature, rare-earth compounds including yttrium tend to form a series of isostructural analogs across the series as, for example, in $R_4Ru_2InGe_4$ (R = La, Ce, Pr, Nd, etc.) [36]. To our surprise, our attempts to synthesize isostructural compounds in $R_7Ru_4InGe_{12}$ (R = Tb, Dy, Ho, Er, Tm, Yb, and Lu) by replacing Y with other rare-earth elements were unsuccessful.

B. Crystal structure

$Y_7Ru_4InGe_{12}$ crystallizes with the $Dy_7Co_4InGe_{12}$-structure type [37] in space group $P4/m$ of the tetragonal system. Other phases reported with this rare structure type are $Dy_7Co_4InGe_{12}$, $Ho_7Co_4InGe_{12}$, $Yb_7Co_4InGe_{12}$, and $Yb_7Ni_4InGe_{12}$ [37,38]. There are eight independent crystallographic sites in the structure of $Y_7Ru_4InGe_{12}$, with three atomic positions for each Y and Ge atom, and one for each Ru and In atom (Table S1 of the SM [27]). They are in the Wyckoff symmetries 4/*m* for Y(2) and In, 2/*m* for Y(3), and *m* for Y(1), Ru, Ge(1), Ge(2), and Ge(3) with full occupancies, which ends up with the refined formula $Y_7Ru_4InGe_{12}$.

The structure of $Y_7Ru_4InGe_{12}$ can be viewed as a dense three-dimensional [Ru_4InGe_{12}] polyanionic network with Y atoms occupied inside three different types of channels. The [Ru_4InGe_{12}] network is composed of pentagonal, hexagonal, and octagonal columns and the Y atoms are located inside each column, as shown in Figs. 1(b) and 1(c). The five-membered rings are formed by two Ge(1) atoms, and each one of Ru, In, and Ge(2) atoms. The six-membered rings consist of two Ge(1)-Ge(2) dimers with intervening Ru atoms. The Ge(1)-Ge(2) bond length is 2.5420(6) Å, which can be considered a single bond. For comparison, a typical single bond length, as found in the modified diamond structure of elemental Ge, is ∼2.45 Å [39], while a double bond length is ∼2.3 Å [40]. The eight-membered rings are composed of alternating Ru and Ge(2) atoms. Note that another smaller tetragonal channel consisting of Ge(3) atoms is penetrated into the octagonal channel via Ru-Ge(3) bonding. The Y(1) atoms are found in the cavities of the pentagonal columns, the Y(2) atoms are located in the centers of the octagons, and the Y(3) atoms are situated in the voids of the hexagonal channels. Due to the channel structure in $Y_7Ru_4InGe_{12}$, the crystal morphology is rodlike with the *c* axis along the rod direction.

The Ru atoms are in square pyramidal geometry and coordinated by five Ge atoms [Fig. 1(d)]. The Ru-Ge bond distances of 2.4026(4)−2.5246(5) Å are within the range of those found in binary Ru_2Ge_3 [2.384(6)−2.664(6) Å] [41]. Each In atom, located at the center of the four adjoining pentagonal channels, possesses a coordination with four Ge(1) atoms at an interatomic distance of 2.9368(5) Å forming a square plane with additional eight Y(1) atoms located above and below the Ge(1) plane [Fig. 1(e)]. Within a radius of 3.5 Å, the coordination numbers of Y(1), Y(2), and Y(3) are 11, 16, and 14, respectively [Figs. 1(f)–1(h)].

C. Superconductivity

The temperature dependence of the resistivity of $Y_7Ru_4InGe_{12}$ along the *c* axis shows metallic behavior above 6 K [Fig. 2(a)]. The resistivity at room temperature is ∼0.079 mΩ cm. There is a sharp superconducting transition (T_c) at ∼5.8 K and zero resistivity is reached at ∼5.6 K with a 0.3 mA current applied [Fig. 2(b)]. Applying a magnetic field along the *ab* plane [Fig. 2(c)] suppresses the transition to lower temperatures and broadens the transitions, particularly for fields larger than 1.3 T, which is most likely due to thermally activated flux motion [42]. Fields larger than 2.1 T suppress the transition below the measurable temperature limit (<1.8 K) of our instrument. The upper critical fields along the *ab* plane based on 90% of normal-state resistivity values are summarized below [Fig. 3(d)]. The normal-state resistivity from 6 to 20 K [Fig. 2(d)] can be well described by the relation $\rho_0 + AT^2$, indicating that electron-electron scattering dominates just above the superconducting transition [43]. The data fitting by the above formula gives $\rho_0 = 0.026\,\mathrm{m\Omega\,cm}$ and $A = 6.2 \times 10^{-6}\,\mathrm{m\Omega\,cm/K^2}$. The

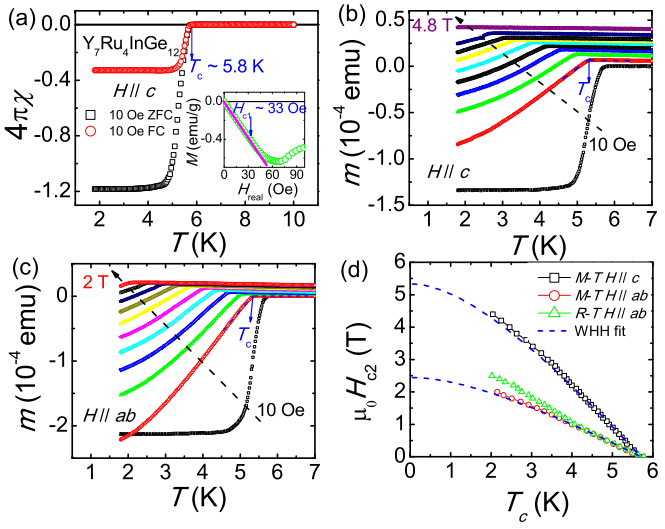

FIG. 3. (a) Temperature dependence of magnetic susceptibility of $Y_7Ru_4InGe_{12}$ crystal under zero-field-cooled (ZFC) and field-cooled (FC) conditions below 10 K. The magnetic field was 10 Oe applied along the c axis. Inset shows field-dependent magnetization from 0 to 100 Oe at 2 K where real magnetic fields were calculated by taking the demagnetization factor. (b),(c) Temperature dependence of magnetic moments of $Y_7Ru_4InGe_{12}$ below 7 K in a ZFC procedure under various magnetic fields in the range of 10 Oe–2 T applied along and perpendicular to the c axis, respectively. The superconducting transition temperatures are extracted from the intersection of two straight lines below and above the transition. (d) Anisotropic upper critical fields extracted from resistivity and magnetization. The temperatures where the normal-state resistivity drops to 90% are used as the superconducting transitions under different fields. The blue dashed lines are the Werthamer-Helfand-Hohenberg (WHH) formula extraction.

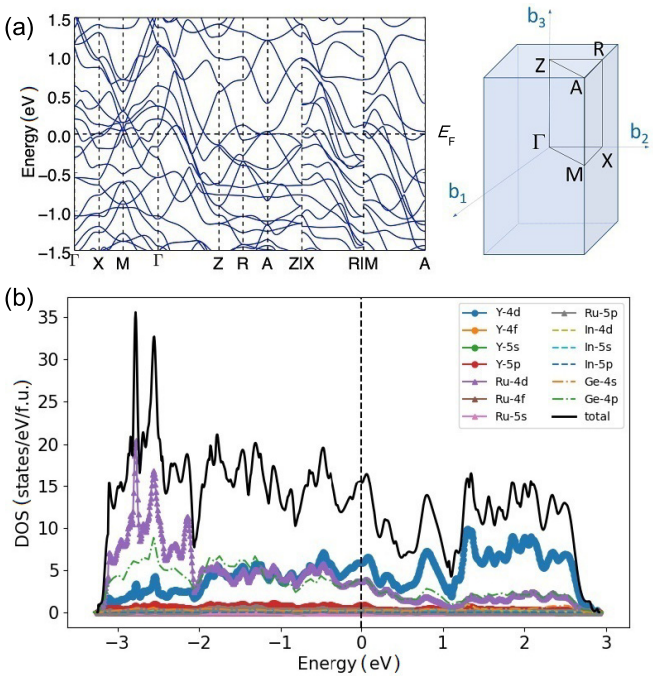

FIG. 4. (a) Electronic band structure of $Y_7Ru_4InGe_{12}$ with high symmetric points labeled on the right panel. (b) Total density of states and projected ones from different atomic orbitals in $Y_7Ru_4InGe_{12}$.

residual resistance ratio (RRR $= \rho_{300\,K}/\rho_0$) of this compound is only ~3, indicating the presence of a considerable number of defects in the sample.

In order to further confirm the bulk nature of superconductivity in $Y_7Ru_4InGe_{12}$, magnetic susceptibility measurements were performed below 10 K in both zero-field-cooled and field-cooled conditions [Fig. 3(a)]. There is a sharp diamagnetic transition at ~5.8 K, consistent with the transition in the resistivity above. The magnetic shielding volume fraction (~1.2) at 2 K exceeds 1, which is most likely due to the underestimation of the demagnetization factor from the irregular sample shape (Fig. S1 in the SM [27]). The magnetic repulsion volume is ~30%, proving the bulk nature of superconductivity and rather weak vortex pinning in $Y_7Ru_4InGe_{12}$. The field dependence of the magnetization at 2 K shows type-II superconductivity in $Y_7Ru_4InGe_{12}$ [Fig. 3(a) inset]. The lower critical field H_{c1} along the c axis at 2 K is ~33 Oe, which was extracted where the magnetization starts to deviate from linear field dependence. The magnetic susceptibility of $Y_7Ru_4InGe_{12}$ shows weak temperature dependence with an upturn at low temperatures, indicating Pauli paramagnetism with some paramagnetic impurities or defects in the sample (Fig. S2 in the SM [27]). The superconducting transition of $Y_7Ru_4InGe_{12}$ moves to lower temperatures when the magnetic fields increase [Figs. 3(b) and 3(c)]. The upper critical fields based on resistivity and magnetization are summarized in Fig. 3(d).

The temperature dependence of the upper critical fields is linear near $T_c \sim 5.8$ K with slopes $\mu_0 \frac{dH}{dT}|_{T\to T_c}$ of -1.35 and -0.62 T/K for the c axis and the ab plane, respectively. The Werthamer-Helfand-Hohenberg (WHH) formula $0.693\mu_0 \frac{dH}{dT}|_{T\to T_c}$ was used to estimate $\mu_0 H_{c2}(0)$ at 0 K where only orbital breaking effects are considered in the dirty limit [44]. The $\mu_0 H_{c2}(0)$ along the c axis and the ab plane were calculated to be ~5.3 and 2.4 T, respectively. These values are much smaller than the Pauli paramagnetic limits ($1.84T_c \sim 10.7$ T) in a BCS weak-coupling case [45,46], indicating that destroying the spin components of the Cooper pairs under magnetic fields is not the dominant pair-breaking effect in $Y_7Ru_4InGe_{12}$. The WHH curves mainly capture the measured upper critical fields with small deviations at low temperatures [Fig. 3(d)]. The anisotropic ratio $\gamma = \frac{H_{c2}^c(0)}{H_{c2}^{ab}(0)}$ in $Y_7Ru_4InGe_{12}$ is ~2.2. According to the formula $\gamma = (\frac{m_{ab}^*}{m_c^*})^{1/2}$, where m_{ab}^* and m_c^* are the effective masses of electrons in the ab plane and along the c axis [47], respectively, the effective mass ratio $\frac{m_{ab}^*}{m_c^*}$ is calculated to be 4.8. This result is qualitatively consistent with the DFT calculations on this compound; see Fig. 4(a). The bands around the Fermi level along the path Γ-Z are much more dispersive than the ones along the paths in the plane such as Γ-X, indicating a smaller effective mass m_c^* along the Γ-Z direction. Based on the anisotropic Ginzburg-Laudau framework, superconducting coherence lengths can be extracted from the following two equations:

$$H_{c2}^c(0) = \frac{\Phi_0}{2\pi\xi_{ab}^2}, \quad H_{c2}^{ab}(0) = \frac{\Phi_0}{2\pi\xi_{ab}\xi_c}, \tag{1}$$

where $\Phi_0 = 2.07 \times 10^{-15}$ Wb is the magnetic quantum flux, and ξ_{ab} and ξ_c are the superconducting coherence length in the *ab* plane and *c* axis [47]. The superconducting coherence ξ_{ab} and ξ_c at 0 K in $Y_7Ru_4InGe_{12}$ were estimated to be 78.8 and 174 Å, respectively. The anisotropy shown above is consistent with the tetragonal channel-like structure in $Y_7Ru_4InGe_{12}$ where conductivity along the shorter *c* axis is expected to be higher than in the *ab* plane. Further accurate quantitative analysis on the anisotropy of resistivity in this material needs to be performed in the future.

The band structure of $Y_7Ru_4InGe_{12}$ shows that more than one electronic band crosses the Fermi level. Y-4*d*, Ru-4*d*, and Ge-4*p* orbital electrons dominate the density of states (DOS) at the Fermi level, while the In-5*p* ones almost have no contribution; see Fig. 4(b). The total DOS of $Y_7Ru_4InGe_{12}$ at the Fermi level is located around a broad peak of ~15.5 states/eV/fu. This may provide enough electron-phonon coupling to drive this compound into a superconducting state similar to the case in the A15 compound [48]. The main charge carriers in $Y_7Ru_4InGe_{12}$ at 10 K are electrons (based on Hall measurements of Fig. S3 in the SM [27]) with a concentration of 6.92×10^{22} cm^{-3} with no sign of a multi-band behavior. Assuming this carrier concentration and a spherical Fermi surface, the mean free path $l_c(0)$ along the *c* axis at 0 K in $Y_7Ru_4InGe_{12}$ is ~29 Å, which is smaller than the coherence length obtained above, proving that the superconductivity of $Y_7Ru_4InGe_{12}$ is in the so-called dirty regime [49]. The superconducting transition temperature of $Y_7Ru_4InGe_{12}$ remains almost the same for different samples with different RRR values; see another sample in Fig. S4 in the SM [27]. Such insensitivity of superconductivity to defects or disorder in $Y_7Ru_4InGe_{12}$ crystals indicates a fully gapped superconducting pairing wave function [50] consistent with specific-heat measurements described below.

The ac specific-heat measurements were carried out on a small sample to investigate the thermodynamic properties of this superconductor. Specific-heat data of $Y_7Ru_4InGe_{12}$ under zero field show a sharp transition at ~5.8 K, further confirming the bulk nature of superconductivity [Fig. 5(a)]. When a magnetic field $\mu_0 H = 5$ T is applied along the *c* axis, the superconducting transition of $Y_7Ru_4InGe_{12}$ was totally suppressed above 1.8 K, consistent with the superconducting phase boundary shown in Fig. 5. The normal-state specific heat was described by the following equation:

$$C_n = \gamma_e T + \beta T^3 + \delta T^5, \tag{2}$$

where $\gamma_e T$ is the electron contribution and $\beta T^3 + \delta T^5$ are the phonon contributions [51]. By fitting the 5 T specific-heat data above 3 K (normal-state curve), we obtained the following parameters: $\gamma_e = 43(1)$ mJ K^{-2} mol-fu^{-1}, $\beta = 3.55(1)$ mJ K^{-4} mol-fu^{-1}, and $\delta = 7.48(1) \times 10^{-3}$ mJ K^{-6} mol-fu^{-1} (fu stands for one formula unit). The Debye temperature Θ of $Y_7Ru_4InGe_{12}$ was estimated to be 236(1) K using the formula $(\frac{12NR\pi^4}{5\beta})^{1/3}$, where N is the number of atoms in one formula unit, R is the gas constant, and β is the coefficient of T^3 in the contribution of phonons. The electron specific heat of $Y_7Ru_4InGe_{12}$ was extracted from the total specific heat by subtracting the phonon contribution [Fig. 5(b)]. The thermodynamic

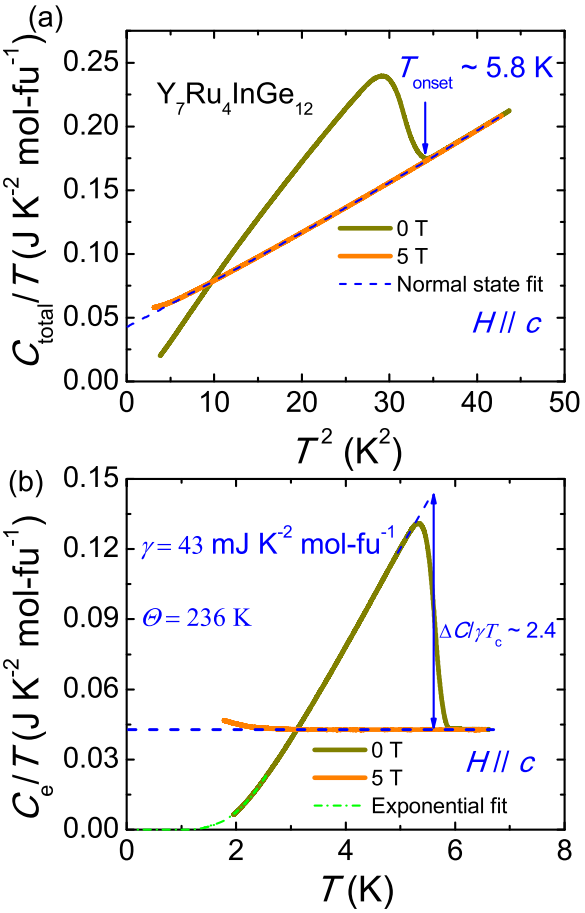

FIG. 5. (a) Specific heat over temperature C_{total}/T vs T^2 measured by the ac specific-heat method. A magnetic field $\mu_0 H = 5$ T was applied along the *c* axis. The blue dashed line represents the normal state of $Y_7Ru_4InGe_{12}$. (b) Electron specific heat over temperature C_e/T vs T after the subtraction of the phonon contribution. The blue dashed line represents the fitted normal-state electronic specific heat. The green dashed line is an exponential decay fit below 2.5 K.

superconducting transition temperature T_c was determined to be 5.6 K by adopting the entropy-conservation criterion, consistent with the zero-resistance temperature shown above. The dimensionless specific-heat jump $\frac{\Delta C}{\gamma_e T_c}$ is ~2.4, much larger than the weak-coupling BCS theoretical value of 1.43, indicating a strong-coupling scenario in $Y_7Ru_4InGe_{12}$, which is similar to the superconductors Pb (~2.77) [52], Nb_3Sn (~2.5) [53], and $K_2Cr_3As_3$ (~2.4) [54]. The electronic specific heat of $Y_7Ru_4InGe_{12}$ under zero applied field below 2.5 K can be well described by an exponential law $a^* e^{-\frac{\Delta(0)}{k_B T}}$ [$\Delta(0)$ is the superconducting gap and k_B is the Boltzmann constant] [55] [see Fig. 5(b)], indicating a fully gapped system with an almost constant energy gap value $\Delta(0) = 1.09(1)$ meV at low temperatures. The gap value is larger than the BCS one of 0.88 meV based on the formula $1.764\, k_B T_c$ in the weak-coupling limit [47], consistent with the strong-coupling scenario in $Y_7Ru_4InGe_{12}$. Assuming an exponential behavior at low temperatures, the superconducting-state electronic entropy S_{es} is still ~10% larger than the normal-state electronic entropy S_{en}; see Fig. 6.

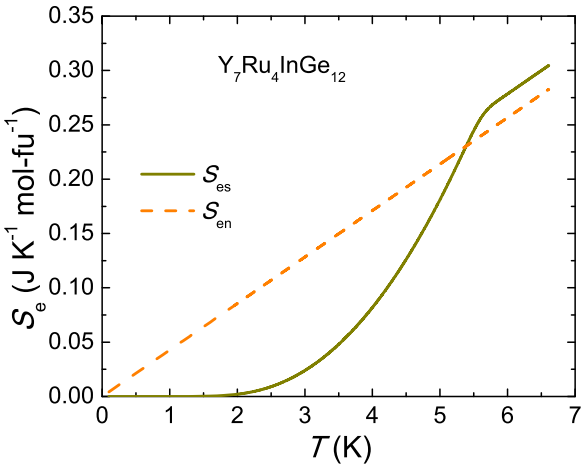

FIG. 6. Temperature dependence of superconducting-state (dark yellow line) and normal-state (orange dash line) electronic entropy in $Y_7Ru_4InGe_{12}$.

The upturn of the normal-state electronic specific heat of $Y_7Ru_4InGe_{12}$ (measured in 5 T) at low temperatures can account for this mismatch. The origin of the upturn could be attributed to several causes such as extrinsic paramagnetic impurities or an inadequate description of the phonon contribution. A Schottky anomaly can be excluded as this normal-state upturn is field independent.

Assuming that superconductivity in $Y_7Ru_4InGe_{12}$ originates only from electron-phonon coupling, the coupling strength λ_{ph} can be estimated from the McMillan formula [56],

$$\lambda_{ph} = \frac{1.04 + \mu^* \ln\left(\frac{\Theta}{1.45T_c}\right)}{(1 - 0.62\mu^*)\ln\left(\frac{\Theta}{1.45T_c}\right) - 1.04}, \quad (3)$$

where μ^* is the Coulomb coupling parameter empirically assigned to 0.13. λ_{ph} in $Y_7Ru_4InGe_{12}$ was estimated to be 0.73, indicating a moderate coupling strength (BCS weak-coupling case: $\lambda_{ph} \ll 1$; strong-coupling case: $\lambda_{ph} > 1$). The inaccurate estimate of λ_{ph} from this formula, compared to the significantly large specific-heat jump, may come from the small value of μ^* where λ_{ph} will increase to 1 if μ^* is chosen to be 0.23. The electron-phonon coupling strength can also be estimated from the experimental specific-heat coefficient γ_e and the DFT-predicted DOS (15.5 states/eV/fu) by the following formula [56]:

$$\gamma_e = \frac{\pi^2}{3k_B^2} N(E)(1 + \lambda_{ph}), \quad (4)$$

where $N(E)$ is the bare DOS from DFT calculations. λ_{ph} is calculated to be 0.18, indicating a rather weak-coupling case in $Y_7Ru_4InGe_{12}$. The discrepancy between the strong-coupling scenario from specific-heat jump and moderate- or weak-coupling electron-phonon coupling estimated from the Debye temperature and electronic specific-heat coefficient suggests an unconventional nature of the electronic properties which requires further detailed investigations of this material by directly estimating λ_{ph} by tunneling measurements [57]. By subtracting the Curie-Weiss tail from the measured magnetic susceptibility at low temperature, we obtained the temperature-independent magnetic susceptibility $\chi = 8.8 \times 10^{-4}$ emu/mol-fu. The Wilson ratio R_w, a value reflecting electron-electron correlations in a material, was calculated by the following equation [58]:

$$R_w = \frac{\pi^2 k_B^2 \chi}{3\mu_0 \mu_B^2 \gamma_e}, \quad (5)$$

where μ_B is the Bohr magneton. The obtained Wilson ratio is around 1.5, which should be close to 1 in a noninteracting Fermi-liquid system [58]. All the superconducting parameters of $Y_7Ru_4InGe_{12}$ are summarized in Table II.

TABLE II. Summary of the superconducting parameters of $Y_7Ru_4InGe_{12}$. T_c is the superconducting transition temperature; $\mu_0 H_{c2}^c(0)$ and $\mu_0 H_{c2}^{ab}(0)$ are the upper critical fields along the c axis and the ab plane at 0 K, respectively; $H_{c1}^c(2\,\mathrm{K})$ is the lower critical field at 2 K; $\gamma(0)$ is the anisotropic ratio of upper critical fields at 0 K; $\xi_c(0)$ and $\xi_{ab}(0)$ are the estimated coherence lengths along the c axis and the ab plane at 0 K, respectively; $l_c(0)$ is the electron mean free path along the c axis; Θ is the Debye temperature; γ_e is the electronic specific-heat coefficient; $\frac{\Delta C}{\gamma_e T_c}$ is the specific-heat jump; $\Delta(0)$ is the superconducting gap from the fitting of specific-heat data at low temperatures; $N(E)$ is the bare density of states at the Fermi level from DFT calculations; χ is the temperature-independent Pauli paramagnetic susceptibility; and R_w is the Wilson ratio.

T_c	5.8 K
$\mu_0 \frac{dH_{c2}^c}{dT}\|_{T\to T_c}$	$-1.35\,\mathrm{T\,K^{-1}}$
$\mu_0 \frac{dH_{c2}^{ab}}{dT}\|_{T\to T_c}$	$-0.62\,\mathrm{T\,K^{-1}}$
$\mu_0 H_{c2}^c(0)$	5.3 T
$\mu_0 H_{c2}^{ab}(0)$	2.4 T
$H_{c1}^c(2\,\mathrm{K})$	33 Oe
$\gamma(0)$	2.2
$\xi_c(0)$	174 Å
$\xi_{ab}(0)$	78.8 Å
$l_c(0)$	29 Å
Θ	236 K
γ_e	$43\,\mathrm{mJ\,K^{-2}\,mol-fu^{-1}}$
$\frac{\Delta C}{\gamma_e T_c}$	2.4
$\frac{2\Delta(0)}{k_B T_c}$	4.36
$N(E)$	$15.5\,\mathrm{states\,eV^{-1}\,fu^{-1}}$
χ	$8.8 \times 10^{-4}\,\mathrm{emu\,mol-fu^{-1}}$
R_w	1.5

IV. CONCLUSION

The quaternary phase $Y_7Ru_4InGe_{12}$ exhibits superconductivity with a transition temperature of ~5.8 K. $Y_7Ru_4InGe_{12}$ shows an anisotropy of 2.2 in the upper critical fields, consistent with the channel-like building blocks in the structure. The large superconducting specific-heat jump $\frac{\Delta C}{\gamma_e T_c}$ (~2.4) points to a strong-coupling scenario in this superconductor. DFT calculations show a broad peak in the density of states around the Fermi level, which may account for the superconductivity probably induced by electron-phonon coupling in this material. Exploration of this intermetallic system with other

rare-earth and transition-metal elements that may reveal isostructural or modified structures could result in new materials exhibiting similar quantum states such as superconductivity and magnetism. Finally, it is also interesting to dope this material with rare-earth elements to introduce $4f$ electrons to study the evolution of superconductivity in this system.

ACKNOWLEDGMENTS

This work was supported by the U.S. Department of Energy, Office of Science, Basic Energy Sciences, Materials Sciences and Engineering Division. EDS/SEM analysis and DFT calculations were carried out at the Center for Nanoscale Materials and the Argonne Leadership Computing Facility, respectively, which are the Office of Science user facilities supported by the U.S. Department of Energy, Office of Science, Office of Basic Energy Sciences, under Contract No. DE-AC02-06CH11357. K.W. acknowledges financial support from the Swiss National Science Foundation through an Early Postdoctorate Mobility fellowship. The authors thank Dr. John Mitchell for his help on measuring the mass of the tiny crystal, and Dr. Daniel Phelan for his helpful discussions on the results.

[1] H. K. Onnes, Commun. Phys. Lab. Univ. Leiden 120b, 122b, 124c (1911).
[2] J. Bardeen, L. N. Cooper, and J. R. Schrieffer, Phys. Rev. **108**, 1175 (1957).
[3] M. R. Norman, Rep. Prog. Phys. **79**, 074502 (2016).
[4] J. E. Hirsch, M. B. Maple, and F. Marsiglio, Phys. C (Amsterdam) **514**, 1 (2015).
[5] J. G. Bednorz and K. A. Müller, Z. Phys. B Con. Mat. **64**, 189 (1986).
[6] Y. Kamihara, T. Watanabe, M. Hirano, and H. Hosono, J. Am. Chem. Soc. **130**, 3296 (2008).
[7] F. Steglich, J. Aarts, C. D. Bredl, W. Lieke, D. Meschede, W. Franz, and H. Schäfer, Phys. Rev. Lett. **43**, 1892 (1979).
[8] M. R. Norman, Science **332**, 196 (2011).
[9] G. R. Stewart, Adv. Phys. **66**, 75 (2017).
[10] E. Pavarini, E. Koch, and P. Coleman (eds.), *Modeling and Simulation, Many-Body Physics: From Kondo to Hubbard* (Forschungszentrum Jülich GmbH Zentralbibliothek, Verlag, 2015), Vol. 5.
[11] D. E. Bugaris, C. D. Malliakas, F. Han, N. P. Calta, M. Sturza, M. J. Krogstad, R. Osborn, S. Rosenkranz, J. P. C. Ruff, G. Trimarchi, S. L. Bud'ko, M. Balasubramanian, D. Y. Chung, and M. G. Kanatzidis, J. Am. Chem. Soc. **139**, 4130 (2017).
[12] H. Bie, O. Y. Zelinska, A. V. Tkachuk, and A. Mar, Chem. Mater. **19**, 4613 (2007).
[13] H. Fujii, T. Okamoto, T. Shigeoka, and N. Iwata, Solid State Commun. **53**, 715 (1985).
[14] J. Chen, K. Semeniuk, Z. Feng, P. Reiss, P. Brown, Y. Zou, P. W. Logg, G. I. Lampronti, and F. M. Grosche, Phys. Rev. Lett. **116**, 127001 (2016).
[15] R. Gumeniuk, W. Schnelle, H. Rosner, M. Nicklas, A. Leithe-Jasper, and Y. Grin, Phys. Rev. Lett. **100**, 017002 (2008).
[16] A. Maisuradze, M. Nicklas, R. Gumeniuk, C. Baines, W. Schnelle, H. Rosner, A. Leithe-Jasper, Y. Grin, and R. Khasanov, Phys. Rev. Lett. **103**, 147002 (2009).
[17] B. K. Rai, I. W. H. Oswald, J. K. Wang, G. T. McCandless, J. Y. Chan, and E. Morosan, Chem. Mater. **27**, 2488 (2015).
[18] K. Ghosh, S. Ramakrishnan, and G. Chandra, Phys. Rev. B **48**, 10435 (1993).
[19] D. Jaccard, K. Behnia, and J. Sierro, Phys. Lett. A **163**, 475 (1992).
[20] A. T. Holmes, D. Jaccard, and K. Miyake, Phys. Rev. B **69**, 024508 (2004).
[21] P. C. Canfield and Z. Fisk, Philos. Mag. B **65**, 1117 (1992).
[22] M. G. Kanatzidis, R. Pöttgen, and W. Jeitschko, Angew. Chem., Int. Ed. **44**, 6996 (2005).
[23] E. L. Thomas, J. N. Millican, E. K. Okudzeto, and J. Y. Chan, Comments Inorg. Chem. **27**, 1 (2006).
[24] S. E. Latturner, Acc. Chem. Res. **51**, 40 (2018).
[25] X-AREA, X-SHAPE, and X-RED (STOE and Cie GmbH, Darmstadt, Germany, 2009).
[26] G. Sheldrick, Acta Crystallogr., Sect. A: Found. Crystallogr. **64**, 112 (2008).
[27] See Supplemental Material at http://link.aps.org/supplemental/10.1103/PhysRevMaterials.3.024802 for details, including tables and figures.
[28] J. A. Osborn, Phys. Rev. **67**, 351 (1945).
[29] S. Tagliati, V. M. Krasnov, and A. Rydh, Rev. Sci. Instrum. **83**, 055107 (2012).
[30] K. Willa, Z. Diao, D. Campanini, U. Welp, R. Divan, M. Hudl, Z. Islam, W. K. Kwok, and A. Rydh, Rev. Sci. Instrum. **88**, 125108 (2017).
[31] R. Dovesi, R. Orlando, B. Civalleri, C. Roetti, V. R. Saunders, and C. M. Zicovich-Wilson, Z. Kristallogr. Cryst. Mater. **220**, 571 (2005).
[32] R. Dovesi, V. Saunders, C. Roetti, R. Orlando, C. Zicovich-Wilson, F. Pascale, K. Doll, N. Harrison, B. Civalleri, and I. Bush, *CRYSTAL09 User's Manual* (University of Torino, Torino, 2009).
[33] J. Laun, D. Vilela Oliveira, and T. Bredow, J. Comput. Chem. **39**, 1285 (2018).
[34] K. Doll and M. Jansen, Angew. Chem. Int. Edit. **50**, 4627 (2011).
[35] G. Venturini, B. Malaman, and B. Roques, J. Less-Common Met. **152**, 51 (1989).
[36] A. O. Oliynyk, S. S. Stoyko, and A. Mar, Inorg. Chem. **54**, 2780 (2015).
[37] M. Chondroudi, M. Balasubramanian, U. Welp, W.-K. Kwok, and M. G. Kanatzidis, Chem. Mater. **19**, 4769 (2007).
[38] U. Subbarao, R. Jana, M. Chondroudi, M. Balasubramanian, M. G. Kanatzidis, and S. C. Peter, Dalton Trans. **44**, 5797 (2015).
[39] J. Donohue, *The Structures of the Elements* (Wiley, New York, 1974).
[40] A. F. Richards, M. Brynda, and P. P. Power, Chem. Commun. (Cambridge), 1592 (2004).

[41] D. J. Poutcharovsky and E. Parthe, Acta Crystallogr., Sect. B: Struct. Sci., Cryst. Eng. Mater. **30**, 2692 (1974).
[42] W. K. Kwok, U. Welp, G. W. Crabtree, K. G. Vandervoort, R. Hulscher, and J. Z. Liu, Phys. Rev. Lett. **64**, 966 (1990).
[43] W. G. Baber, P. Roy. Soc. Lond. A Mat. **158**, 383 (1937).
[44] N. R. Werthamer, E. Helfand, and P. C. Hohenberg, Phys. Rev. **147**, 295 (1966).
[45] B. S. Chandrasekhar, Appl. Phys. Lett. **1**, 7 (1962).
[46] A. M. Clogston, Phys. Rev. Lett. **9**, 266 (1962).
[47] M. Tinkham, *Introduction to Superconductivity*, 2nd ed. (Dover, Mineola, NY, 2004).
[48] G. R. Stewart, Physica C **514**, 28 (2015).
[49] R. D. Parks, *Superconductivity* (Marcel Dekker, New York, 1969), Vol. 2.
[50] P. W. Anderson, J. Phys. Chem. Solids **11**, 26 (1959).
[51] T. C. Cetas, C. R. Tilford, and C. A. Swenson, Phys. Rev. **174**, 835 (1968).
[52] J. P. Carbotte, Rev. Mod. Phys. **62**, 1027 (1990).
[53] V. Guritanu, W. Goldacker, F. Bouquet, Y. Wang, R. Lortz, G. Goll, and A. Junod, Phys. Rev. B **70**, 184526 (2004).
[54] J.-K. Bao, J.-Y. Liu, C.-W. Ma, Z.-H. Meng, Z.-T. Tang, Y.-L. Sun, H.-F. Zhai, H. Jiang, H. Bai, C.-M. Feng, Z.-A. Xu, and G.-H. Cao, Phys. Rev. X **5**, 011013 (2015).
[55] E. S. R. Gopal, *Specific Heats at Low Temperatures* (Prenum, New York, 1966).
[56] W. L. McMillan, Phys. Rev. **167**, 331 (1968).
[57] P. Samuely, N. L. Bobrov, A. G. M. Jansen, P. Wyder, S. N. Barilo, and S. V. Shiryaev, Phys. Rev. B **48**, 13904 (1993).
[58] G. R. Stewart, Rev. Mod. Phys. **56**, 755 (1984).